



# Design of MoFe/Beta@CeO<sub>2</sub> catalysts with a core–shell structure and their catalytic performances for the selective catalytic reduction of NO with NH<sub>3</sub>



Jixing Liu<sup>a</sup>, Yuhao Du<sup>a</sup>, Jian Liu<sup>a,\*</sup>, Zhen Zhao<sup>a</sup>, Kai Cheng<sup>a</sup>, Yongsheng Chen<sup>b</sup>, Yuechang Wei<sup>a</sup>, Weiyu Song<sup>a</sup>, Xiao Zhang<sup>a</sup>

<sup>a</sup> State Key Laboratory of Heavy Oil Processing and Beijing Key Lab of Oil & Gas Pollution Control, China University of Petroleum, Beijing 102249, PR China

<sup>b</sup> William M.W. Mong Engineering Building Chinese University of Hong Kong, Shatin, N.T. Hong Kong SAR, PR China

## ARTICLE INFO

### Article history:

Received 18 July 2016

Received in revised form

20 September 2016

Accepted 14 October 2016

Available online 15 October 2016

### Keywords:

MoFe/Beta

CeO<sub>2</sub>

Core–shell

SO<sub>2</sub> tolerance

Selective catalytic reduction

## ABSTRACT

MoFe/Beta@CeO<sub>2</sub> core–shell catalyst was designed with nano-size Beta supporting MoFe bimetallic oxides as the core and CeO<sub>2</sub> thin film as the shell. The structure and physico-chemical properties of the coated and uncoated CeO<sub>2</sub> catalysts were characterized by TEM, SEM, XRD, N<sub>2</sub> adsorption–desorption, XPS, XANES, ICP-AES, NH<sub>3</sub>-TPD, H<sub>2</sub>-TPR and in-situ DRIFTS. The catalytic activity tests for NH<sub>3</sub>-SCR of NO indicated that the catalyst coated by CeO<sub>2</sub> shell exhibits a remarkable improvement of deNO<sub>x</sub> activity, excellent tolerance to SO<sub>2</sub> and H<sub>2</sub>O, as well as high thermal stability. The both chemisorbed oxygen species (O<sub>2</sub><sup>–</sup>, O<sup>2–</sup>) and specific surface area increased for the catalysts after the coating of CeO<sub>2</sub> shells. CeO<sub>2</sub> shells not only increase the acid amount but also improve its acid strength, which could be beneficial to improving NO oxidation to NO<sub>2</sub> during NH<sub>3</sub>-SCR. Furthermore, there is a strong interaction among the iron oxides, molybdenum oxides and CeO<sub>2</sub> shells. CeO<sub>2</sub> shells can serve as an effective barrier to inhibit the active metal oxides nanoparticles from aggregating at high temperature. As a result, the coated catalyst with CeO<sub>2</sub> thin film shows a better thermal stability than the uncoated one. What's more, CeO<sub>2</sub> shells can not only suppress the formation of ammonium nitrate and sulfate species blocking the active iron sites but also restrain the generation of iron sulfate, leading to a higher SO<sub>2</sub> and H<sub>2</sub>O-tolerance. The above results demonstrate that the design of a core–shell structure catalyst is favorable for improving the performance of deNO<sub>x</sub> catalysts.

© 2016 Elsevier B.V. All rights reserved.

## 1. Introduction

Nitrogen oxides (NO<sub>x</sub>) originating from mobile sources, especially the diesel vehicles, contribute greatly to air pollution [1]. So far, the selective catalytic reduction (SCR) of NO<sub>x</sub> with NH<sub>3</sub> is considered as the most promising technology [2]. The typically commercial V<sub>2</sub>O<sub>5</sub>-WO<sub>3</sub>(MoO<sub>3</sub>)/TiO<sub>2</sub> catalysts for NH<sub>3</sub>-SCR have been widely used for decades [3]. Nevertheless, some inevitable disadvantages still remain, for instance, the toxicity of vanadium species, the poor low-temperature catalytic activity, the low N<sub>2</sub> selectivity and the high activity for oxidation of SO<sub>2</sub> to SO<sub>3</sub>. These factors greatly restrict its application for the deNO<sub>x</sub> process in industry [4,5]. Therefore, it is necessary to develop V-free

deNO<sub>x</sub> catalysts with high catalytic activity, excellent H<sub>2</sub>O and SO<sub>2</sub>-tolerance, as well as high thermal stability [6,7].

Zeolite-based materials, such as SSZ-13 [8], SAPO-34 [9], ZSM-5 [10], FAU [11], HBFA [12], MOR [13] and USY [14], have attracted much attention due to their good adsorption performance and flexibility in active temperature window. There is a significant interest in developing zeolite-based catalysts for NH<sub>3</sub>-SCR. Meanwhile, attracted by their superior SCR performance and N<sub>2</sub> selectivity in a wide operation temperature range, Fe exchanged zeolite have been extensively studied in the NH<sub>3</sub>-SCR reaction over the past decades [9,15–17]. However, the low-temperatures catalytic activity of Fe-based catalysts still needs improvement [18,19]. What's more, the high concentration of SO<sub>2</sub> in the diesel vehicle exhaust can lead to the loss of the active Fe oxides species [20]. Consequently, SO<sub>2</sub> poisoning is a great challenge for the preparation of high activity of low-temperature NH<sub>3</sub>-SCR catalyst. Molybdenum, which is usually introduced as a promoter for improving catalytic activity and enhancing SO<sub>2</sub> resistance due to its unique redox property, has been

\* Corresponding author. Postal Address: 18# Fuxue Road, Chang Ping District, Beijing, 102249, PR China.

E-mail address: [liujian@cup.edu.cn](mailto:liujian@cup.edu.cn) (J. Liu).

reported in many fields [21–23]. It is also promising to improve the ability of SO<sub>2</sub>-resistance and stability of FeO<sub>x</sub> metal oxide catalysts.

Core–shell catalysts (CSCs), constituted with cores (inner materials) and shells (outer layer materials), have drew enormous attention due to their interesting properties as well as utility in the diverse areas including nano-catalysis, magnetite-supported catalysis, nano-electronics, integrated catalysis, etc [24,25]. In most cases, the CSCs show superior properties than either core or shell material alone. For example, Mitsudome et al. [26] reported AgNPs@CeO<sub>2</sub> CSCs to be employed in the reaction of nitrobenzene reduction, which exhibited better catalytic activity than Ag NPs (nanoparticles) alone due to the fact that the presence of CeO<sub>2</sub> can prevent the migration and agglomeration of Ag NPs. Zhang et al. [27] prepared a *meso*-TiO<sub>2</sub>@MnCe/CNTs core–shell catalyst to be used in NH<sub>3</sub>-SCR reaction. The results revealed that the *meso*-TiO<sub>2</sub> sheaths greatly improve the SCR activity, SO<sub>2</sub>-tolerance and stability of the coated catalyst compared with the uncoated one. Nevertheless, the hydrothermal stability of this catalyst is so poor that it is easy to be collapsed at the high reaction temperature (>500 °C) [28]. What's more, the weak acid of CNTs (carbon nanotubes) is unfavorable for the adsorption and activation of NH<sub>3</sub>. In contrast, Beta zeolite possesses a stronger acidity and better hydrothermal stability. Moreover, compared with the CHA-zeolite catalysts, Beta zeolite possesses a larger pore size, which is not readily blocked by the outer oxide shell. Therefore, it can enhance the access of reactant molecules to the catalytically active center. Of course, as the core materials, the size of Beta crystal should be as small as possible. For the selection of shell materials, CeO<sub>2</sub> may be one of the most suitable metal oxides owing to its outstanding oxygen storage and oxidation-reduction properties, which has been extensively used in various catalytic reactions [29–32]. Furthermore, NH<sub>3</sub>-SCR is also an acid catalysis reaction. The thicker of the coated oxide film, the weaker of the catalyst acidity. Thus, the suitable thickness of CeO<sub>2</sub> oxide film is of importance for high NH<sub>3</sub>-SCR activity.

Herein, a core–shell structural deNO<sub>x</sub> catalyst, nano-size Beta supporting MoO<sub>x</sub> and FeO<sub>x</sub> bimetallic NPs as the core and CeO<sub>2</sub> thin film as sheaths, was demonstrated an excellent catalytic performances and high stability for H<sub>2</sub>O and SO<sub>2</sub>-tolerance. In this design, CeO<sub>2</sub> sheath not only restrain the formation of ammonium nitrate and sulfate species blocking the active iron sites but also prevents from the generation of iron sulfate. Moreover, CeO<sub>2</sub> sheath can provide an effective barrier to suppress the migration and agglomeration of active metal oxide NPs during the deNO<sub>x</sub> process. The catalysts show the high stability and SO<sub>2</sub>-tolerance. Thus, the excellent catalytic performances are obtained.

## 2. Experimental

### 2.1. Preparation of materials

The preparation process of MoFe/Beta@CeO<sub>2</sub> core–shell structure includes three steps as illustrated in **Scheme 1**. The first step involved the preparation of nano-size of HBeta crystals. The second one referred to the supporting of MoO<sub>x</sub> and FeO<sub>x</sub> NPs. Then, the Beta loaded with metal oxide NPs were then used as the support for the coating of CeO<sub>2</sub> sheaths.

Nano-size Beta (SiO<sub>2</sub>/Al<sub>2</sub>O<sub>3</sub> = 30) crystals were synthesized by the following chemical composition: 1.4 Na<sub>2</sub>O: 18 (TEA)<sub>2</sub>O: 1 Al<sub>2</sub>O<sub>3</sub>: 100 SiO<sub>2</sub>: 1180H<sub>2</sub>O. A certain amount of tetraethylammonium hydroxide (TEAOH, 25 wt%), deionized water, silica sol (40 wt%), aluminum isopropoxide (98%) and sodium hydroxide (>96%) were mixed under vigorous stirring for 24 h and then the gel was sealed into an autoclave and hydrothermal treatment at 100 °C for 3 days. The product was obtained by washed with deionized water for more than three times, dried in air and calcined at

550 °C for 6 h to get Na-Beta. H-Beta was obtained by treating Na-Beta with 0.1 mol/L NH<sub>4</sub>NO<sub>3</sub> at 80 °C for 8 h under vigorous stirring, then the H-Beta was dried in air and calcined at 450 °C for 3 h.

MoFe/Beta catalyst was synthesized by an improved incipient wetness impregnation method using the above nano-size H-Beta zeolite as the catalyst support. In a typical synthesis, 1 g H-Beta powders was mixed with required amounts of Fe(NO<sub>3</sub>)<sub>3</sub>·9H<sub>2</sub>O (0.18 g) and (NH<sub>4</sub>)<sub>6</sub>Mo<sub>7</sub>O<sub>24</sub>·4H<sub>2</sub>O (0.006 g) solution and bath ultrasounded in an ultrasound generator (70 W) for 4 h at room temperature, then evaporated water and dried in air followed by calcined at 550 °C for 4 h. The obtained nanocomposites are denoted as MoFe/Beta.

For MoFe/Beta@CeO<sub>2</sub> core–shell catalyst, 100 mg of as-prepared MoFe/Beta nanocomposite was dispersed in a 100 mL mixed solution of water/ethanol (v/v = 1), then, 1 g polyvinylpyrrolidone (PVP) powder was added in the above solution and stirred until completely dissolved. Subsequently, 0.08 g Ce(NO<sub>3</sub>)<sub>3</sub> and 0.06 g of hexamethylenetetramine were added in turn, and continued to stir and reflux for 2 h at 60 °C. The product was obtained by centrifugation, washed with deionized water and ethanol, dried in air, followed by calcination in an inert environment at 500 °C for 3 h. The final product was denoted as MoFe/Beta@CeO<sub>2</sub>.

For comparison, CeMoFe/Beta with the same Ce content as MoFe/Beta@CeO<sub>2</sub> core–shell catalyst was prepared by a conventional incipient wetness impregnation method. Pure CeO<sub>2</sub> NPs was synthesized as follows: 100 mg Ce(NO<sub>3</sub>)<sub>3</sub> was dissolved in 100 mL mixed solution of water/ethanol (v/v = 1), and then 1 g PVP powder and 0.06 g HMT were introduced in turn. The mixture was heated to 60 °C and refluxed at this temperature for 2 h before being cooled down to room temperature. The final product was obtained by centrifugation, washed with deionized water and ethanol, dried in air. Finally, the product was calcined in an inert environment at 500 °C for 3 h.

Cu/SAPO-34 was synthesized by the following two-step ion-exchange (IE) process. H-SAPO-34 was prepared according to the procedure described in Ref [33]. First, an IE step was employed using an excess amount of 0.1 mol/L NH<sub>4</sub>NO<sub>3</sub> at 50 °C for 5 h to generate NH<sub>4</sub>/SAPO-34. Subsequently, centrifugation separation and washing cycles were applied. Then, NH<sub>4</sub>/SAPO-34 was further exchanged with 0.01 mol/L Cu(OAc)<sub>2</sub> at 50 °C for 1 h to generate the resulting Cu/SAPO-34 (~2.0 wt% Cu). Finally, the as-synthesized Cu/SAPO-34 was separated, washed and dried at 110 °C, and then calcined at 550 °C for 4 h.

### 2.2. Characterization of catalysts

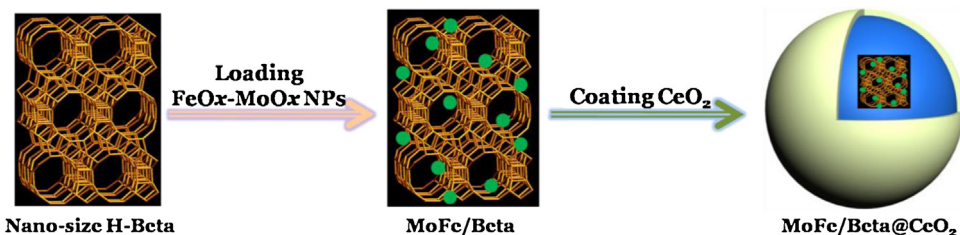
High resolution transmission electron microscopy (HRTEM) micrographs were conducted on a Tecnai G2 F20 electron microscope equipped with a field emission source operating at 200 kV. The elemental local, mapping and line-scanning analyses were collected by energy dispersive spectroscopy (EDS) using a Tecnai F20 electron microscope.

Scanning electron microscopy (SEM) measurements were obtained on an FEI Quanta 200F instruments with the working voltages of 5 kV.

Powder X-ray diffraction (XRD) pattern was performed on a Bruker D8 Advance diffractometer equipped with Cu K<sub>α</sub> radiation in the 2θ range of 5–70° and scanning rate of 2°/min.

N<sub>2</sub> adsorption-desorption isotherms were recorded with a Micromeritics TriStar II 3020 porosimetry analyzer at 77 K.

X-ray photoelectron spectroscopy (XPS) spectra were collected on a PerkinElmer PHI-1600 ESCA spectrometer equipped with Mg K<sub>α</sub> (hv = 1253.6 eV) radiation. The binding energies were calibrated using C1 s peak of contaminant carbon (BE = 284.6 eV) as an internal standard. Deconvolution of Fe 2p, Mo 3d, O 1 s and Ce 3d peak of catalysts was performed by using origin 7.0 software.



**Scheme 1.** Schematic illustration of the formation of MoFe/Beta@CeO<sub>2</sub> core-shell catalyst.

X-ray absorption near edge structure (XANES) of Fe L<sub>3</sub>-edge spectra were recorded at Beamline 9-BM of Advanced Photon Source (APS), Argonne National Laboratory. The monochromator was double-crystal Si (111), and the XANES spectra were collected in fluorescence mode with a Si DRIFT 4-element detector (Vortex). Harmonics were rejected using an Rh-coated flat mirror in the experimental station.

The element content of as-prepared materials was determined by a Varian 715-ES inductively coupled plasma-atomic emission spectrometer (ICP-AES).

Temperature-programmed desorption of ammonia (NH<sub>3</sub>-TPD) measurements were conducted on a conventional flow apparatus. Prior to each test, 0.1 g of the catalyst was purged by a flowing N<sub>2</sub> (40 mL/min) at 600 °C for 30 min, and then the sample was cooled down to 100 °C. Subsequently, ammonia was adsorbed at this temperature for 30 min to ensure the sufficient adsorption of NH<sub>3</sub>. Before desorption, the sample was purged by a flowing He stream at 100 °C for 1 h to remove excessive and physically adsorbed NH<sub>3</sub>. Finally, the sample was heated from 100 to 500 °C at a rate of 10 °C/min in a pure N<sub>2</sub> (40 mL/min) flow and desorption pattern was recorded.

Temperature programmed reduction of hydrogen (H<sub>2</sub>-TPR) experiment was conducted on a ChemiSorb2720 TPx chemisorption analyzer. Prior to reduction, 50 mg of the catalyst was purged by a flowing N<sub>2</sub> (40 mL/min) at 600 °C for 30 min, and then the sample was cooled down to 60 °C in a N<sub>2</sub> flow. The temperature programmed reduction process was performed in flow of 10% H<sub>2</sub>/N<sub>2</sub> (40 mL/min) up to 900 °C at a rate of 10 °C/min.

In-situ DRIFTS experiments were carried out on an FTIR spectrometer equipped with an MCT/A detector and a ZnSe window. The catalyst (about 0.1 g) was loaded in a Harrick IR cell and heated to 500 °C under N<sub>2</sub> purging at a total flow rate of 100 mL/min for 1 h to remove adsorbed impurities. A background spectrum was collected under a flowing N<sub>2</sub> atmosphere and was subtracted from the sample spectra. DRIFTS were recorded by accumulating 32 scans with a resolution of 4 cm<sup>-1</sup>.

### 2.3. Activity evaluation

NH<sub>3</sub>-SCR activity of the catalysts was evaluated on a fixed-bed micro-reactor operated in a steady flow mode. The typical reaction condition was as follows: [NH<sub>3</sub>] = [NO] = 500 ppm, [SO<sub>2</sub>] = 100 ppm, [O<sub>2</sub>] = 3 vol%, 10% H<sub>2</sub>O, N<sub>2</sub> balance and 500 mL/min total gas flow rate. 0.4 g catalyst (40–60 mesh) was employed. Therefore, the employed gas hourly space velocity (GHSV) was about 50,000 h<sup>-1</sup> for each activity test. The concentration of NO<sub>x</sub> (NO<sub>x</sub> = NO + NO<sub>2</sub>) in the inlet and outlet gas at steady-state was measured using a flue gas analyzer (Model-4000VM, SIGNAL international Ltd., UK), and NH<sub>3</sub> and N<sub>2</sub>O was monitored by a NEXUS 670-FTIR spectrometer. The NO<sub>x</sub> conversion and N<sub>2</sub> selectivity were calculated using the following equations:

$$\text{NO}_x \text{ conversion} = \frac{[\text{NO}_x]_{\text{inlet}} - [\text{NO}_x]_{\text{outlet}}}{[\text{NO}_x]_{\text{inlet}}} \times 100\% \quad (1)$$

$$\text{N}_2 \text{ Selectivity} = \left( 1 - \frac{2[\text{N}_2\text{O}]_{\text{outlet}}}{[\text{NO}_x]_{\text{inlet}} + [\text{NH}_3]_{\text{inlet}} - [\text{NO}_x]_{\text{outlet}} - [\text{NH}_3]_{\text{outlet}}} \right) \times 100\% \quad (2)$$

## 3. Results and discussion

### 3.1. TEM results

The morphology and shell structure of the as-prepared MoFe/Beta@CeO<sub>2</sub> was investigated by TEM and HRTEM combined with EDS elemental mapping and line analyses. As exhibited in Fig. 1a, through the self-assembly method, the outer surface of MoFe/Beta@CeO<sub>2</sub> was successfully covered by a thin metal oxides “layer”. As shown in Fig. 1b, HRTEM image shows that the shell-thickness is around 10 nm. Moreover, the property of the shell was further analyzed by selected-area electron diffraction, and the corresponding SAED pattern reveal the diffraction spots from (111), (200), (220), (311), which is attributed to CeO<sub>2</sub> fluorite crystalline features (Fig. 1c). Furthermore, the STEM image of a single MoFe/Beta@CeO<sub>2</sub> microsphere combined with EDX elemental mapping and line scanning analyses (Fig. 1e–h), clearly reveals the core–shell structure of MoFe/Beta@CeO<sub>2</sub>. Therefore, as expected, the core–shell structure of MoFe/Beta@CeO<sub>2</sub> has been successfully prepared by this simple self-assembly method.

### 3.2. SEM results

SEM was performed to further insight into the change of the morphology of sample before and after coated by CeO<sub>2</sub> shell and the results are elucidated in Fig. 2. It was obviously noted that MoFe/Beta (Fig. 2a) is composed of egg-like aggregates with diameters around 100 nm, and that the surface of the catalyst is rough and decorated with numerous metal oxide NPs. By contrast, the surface of MoFe/Beta@CeO<sub>2</sub> becomes rougher after CeO<sub>2</sub> coating. EDS elemental analysis for MoFe/Beta@CeO<sub>2</sub> (Fig. 2b) shows that the content of Ce is 12.54 wt%. Fig. 2c shows HAADF-STEM images of MoFe/Beta@CeO<sub>2</sub> together with the elemental mapping images for Si, Al, O, Fe, Mo and Ce. From the elemental mapping image of Mo and Fe, it is clearly seen that Mo, Fe and Ce species are highly dispersed on the supports.

### 3.3. XRD results

In order to determine the phases and chemical compositions on MoFe/Beta@CeO<sub>2</sub>, CeMoFe/Beta, MoFe/Beta and pure CeO<sub>2</sub>, XRD detection was carried out, and the results are demonstrated in Fig. 3. For MoFe/Beta@CeO<sub>2</sub> (Fig. 3a), the diffraction peaks at 2θ = 7.6, 14.7 and 22.4° can be ascribed to the characteristic reflections of Beta [18]. While the weak diffraction peaks at 2θ = 28.6 and 33.0° can be indexed to the diffraction peaks of CeO<sub>2</sub> with the fcc fluorite structure [34,35]. Moreover, the diffraction peaks intensity corresponding to Beta zeolite remarkably decreases due to the modification of CeO<sub>2</sub> compared with MoFe/Beta, in agreement with its core (MoFe/Beta)@shell (CeO<sub>2</sub>) nanostructure [36]. CeMoFe/Beta (Fig. 3b) exhibits similar diffraction peaks with

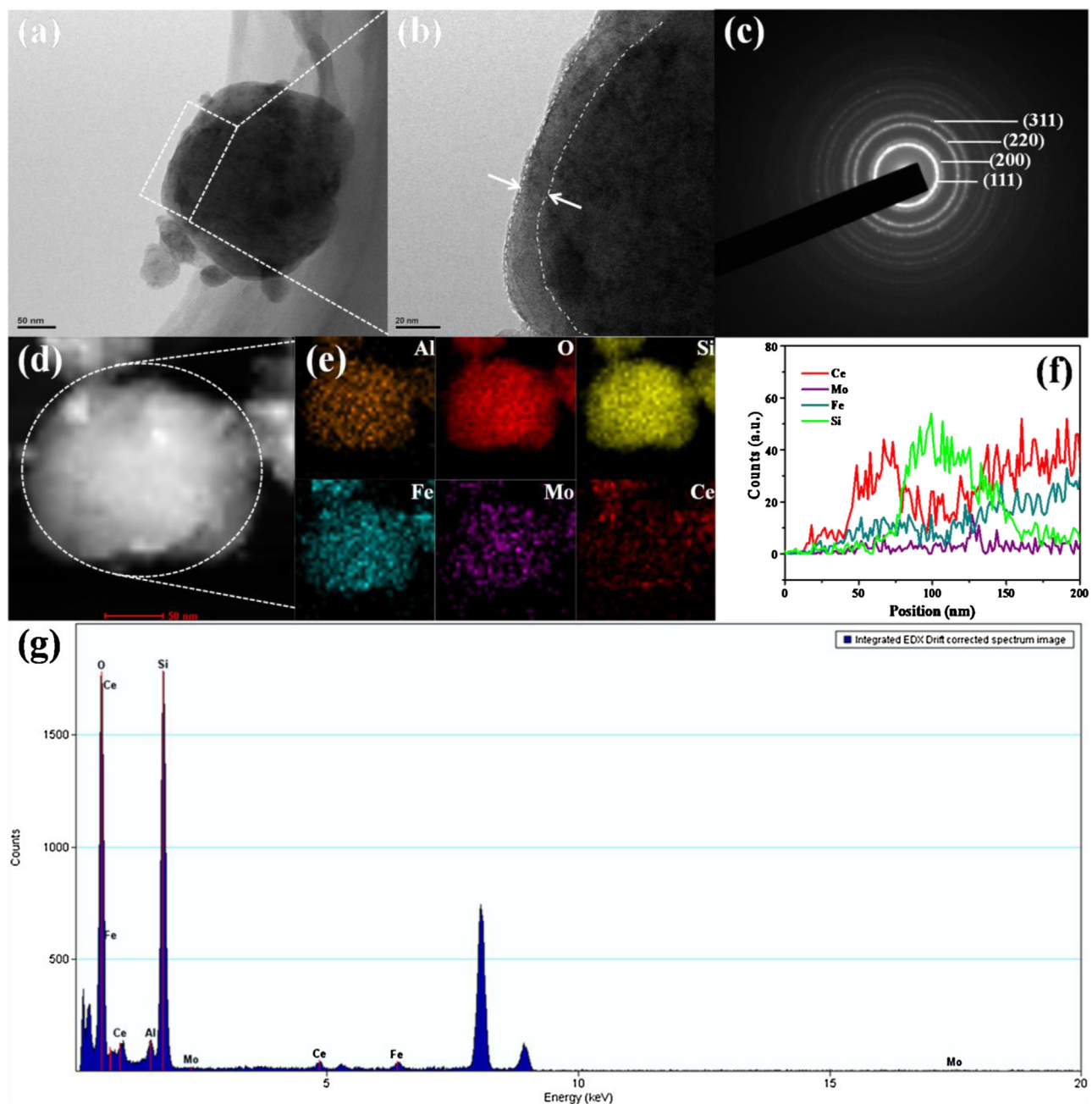


**Fig. 1.** (a) TEM image of MoFe/Beta@CeO<sub>2</sub> (b) HRTEM image of MoFe/Beta@CeO<sub>2</sub> (c) the SAED pattern of MoFe/Beta@CeO<sub>2</sub> (d) the STEM image of a single MoFe/Beta@CeO<sub>2</sub> microsphere; (e) the mapping elemental analyses for MoFe/Beta@CeO<sub>2</sub> (f) the line scanning of a typical particle and (g) EDS data of the single MoFe/Beta@CeO<sub>2</sub> microsphere.

MoFe/Beta@CeO<sub>2</sub> core–shell catalyst. The obviously differences are that the intensity of the characteristic diffraction peaks ascribed to Beta grows stronger, and several new peaks ascribed to CeO<sub>2</sub> appear, indicating that CeO<sub>2</sub> NPs distributed more homogeneously on MoFe/Beta@CeO<sub>2</sub> than on CeMoFe/Beta, which may be beneficial to the selective catalytic reduction of NO.

### 3.4. N<sub>2</sub> adsorption-desorption results

N<sub>2</sub> adsorption-desorption was carried out to investigate the change of the porous structure and specific surface area before and after coating with CeO<sub>2</sub> layers, and the results are shown in Fig. 4. It can be seen that the samples of MoFe/Beta@CeO<sub>2</sub>, CeMoFe/Beta and MoFe/Beta are type-I isotherm, characteristic microporous materials [37]. While CeO<sub>2</sub> exhibits type-IV isotherms and typi-

**Table 1**  
Surface area and pore volume of catalysts.

Samples	$A_{\text{BET}}^{\text{a}}$ (m <sup>2</sup> /g)	$V_t^{\text{b}}$ (mL/g)	$A_{\text{Ext}}^{\text{a}}$ (m <sup>2</sup> /g)	$V_{\text{Meso}}$
MoFe/Beta@CeO <sub>2</sub>	402.0	0.251	134.9	0.140
CeMoFe/Beta	385.1	0.201	112.4	0.083
MoFe/Beta	362.7	0.203	131.3	0.107
CeO <sub>2</sub>	95.4	0.294	48.2	0.285

<sup>a</sup> Calculated by BET method.

<sup>b</sup> Calculated by *t*-plot method.

cal H<sub>2</sub> hysteresis loops, reflecting the mesoporous structure of the catalyst. Their BET surface areas and pore volumes are summarized in Table 1. The specific surface area ( $A_{\text{BET}}$ ) and pore volume ( $V_t$ ) of MoFe/Beta@CeO<sub>2</sub> is 402.0 m<sup>2</sup>/g and 0.251 mL/g, respectively. It is obviously larger than that of MoFe/Beta (362.7 m<sup>2</sup>/g

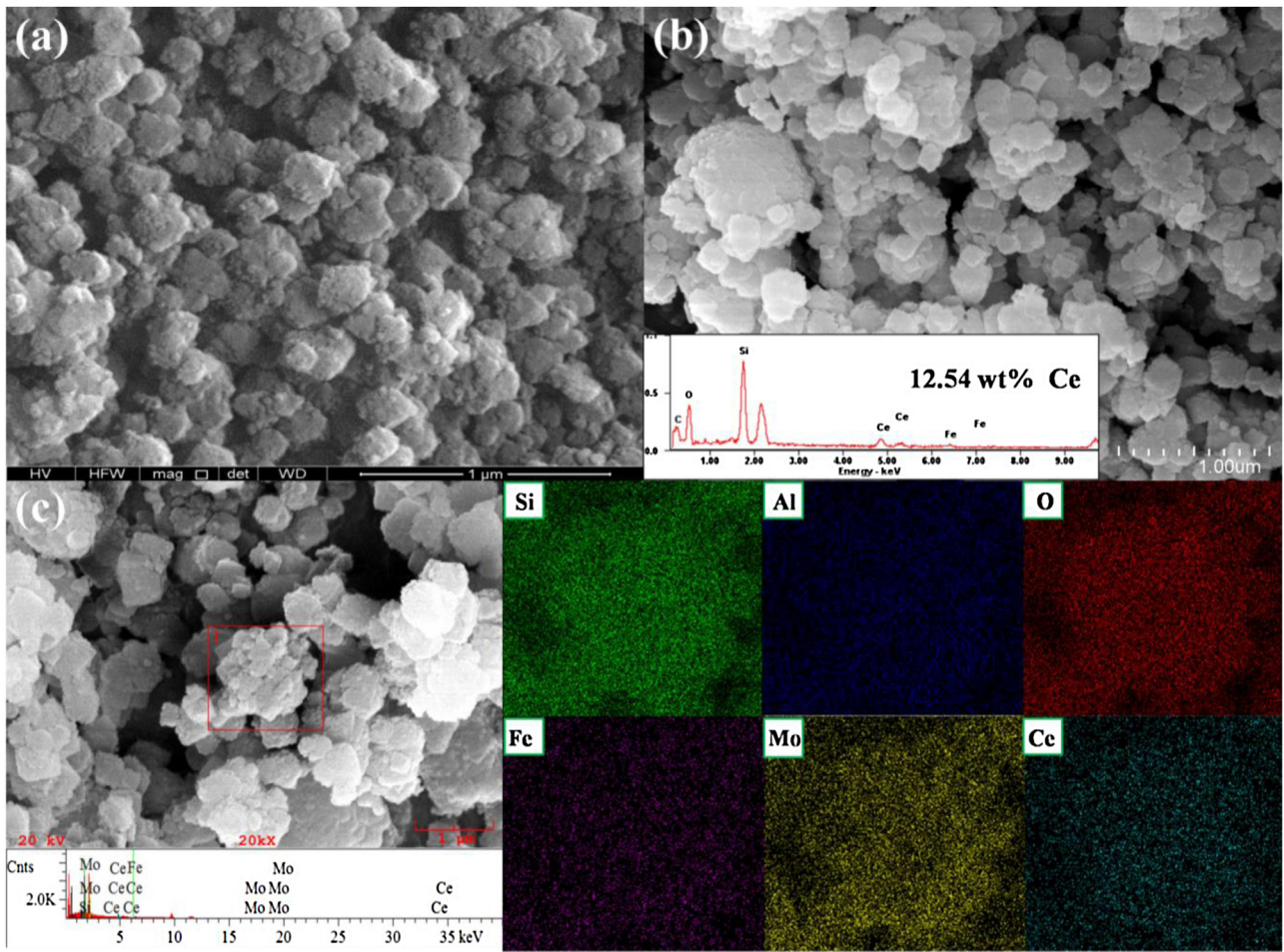


**Fig. 2.** SEM images of the catalysts: (a) MoFe/Beta and (b) MoFe/Beta@CeO<sub>2</sub> and (c) HAADF-STEM image and EDS elemental analyses for MoFe/Beta@CeO<sub>2</sub>.

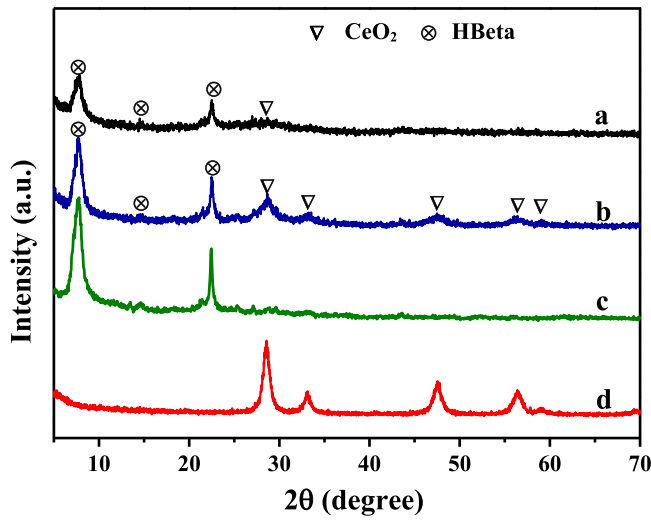


**Fig. 3.** XRD patterns of the catalysts: (a) MoFe/Beta@CeO<sub>2</sub> (b) CeMoFe/Beta (c) MoFe/Beta and (d) CeO<sub>2</sub>.

and 0.203 mL/g), which may be due to the formation of mesopores resulting from the coating with CeO<sub>2</sub> layer. The mesoporous feature of CeO<sub>2</sub> shells is beneficial to the transport of reactant molecules and necessary to improve the accessibility of reactants to catalytic active sites, which is evidenced by the catalytic performance of MoFe/Beta@CeO<sub>2</sub> below. In addition, it's noted that CeMoFe/Beta

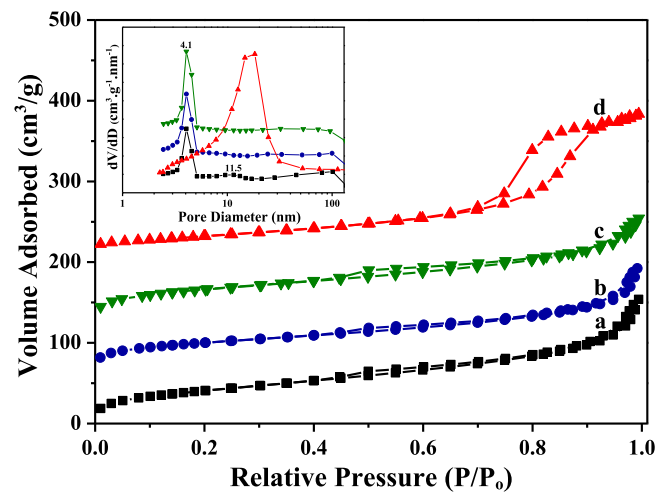


**Fig. 4.** (A) Nitrogen adsorption-desorption isotherms and (B) the size distribution curves of the catalysts: (a) MoFe/Beta@CeO<sub>2</sub> and (b) CeMoFe/Beta (c) MoFe/Beta and (d) CeO<sub>2</sub>.

exhibit a similar pore volume with MoFe/Beta. While the external surface area ( $A_{Ext}$ ) and mesoporous pore volume ( $V_{Meso}$ ) are smaller than those of MoFe/Beta due to the deposition of CeO<sub>2</sub>. The pore size distribution which is calculated with the BJH model is exhibited in Fig. 4 (inset). It can be observed that all of MoFe/Beta@CeO<sub>2</sub>, CeMoFe/Beta and MoFe/Beta catalysts show similar pore distribu-

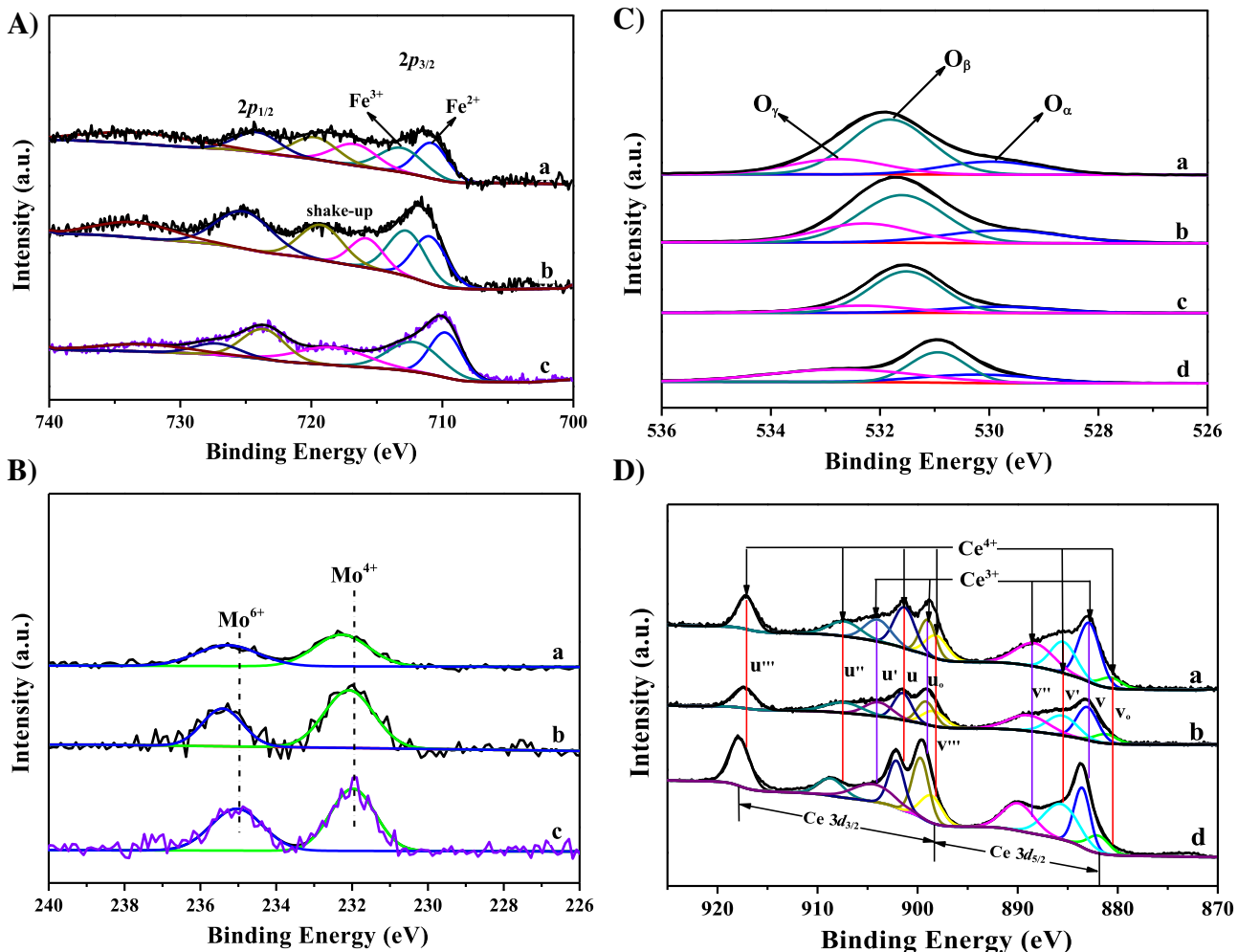


**Fig. 5.** XPS spectra of (A) Fe 2p, (B) Mo 3d (C) O 1s and (D) Ce 3d of the catalysts: (a) MoFe/Beta@CeO<sub>2</sub> (b) CeMoFe/Beta (c) MoFe/Beta (d) CeO<sub>2</sub>.

tion. It reveals that the coating of CeO<sub>2</sub> shell didn't damage the initial structure of MoFe/Beta, which is consistent with XRD results. In addition, a weak pore size around at 11.5 nm is observed over MoFe/Beta@CeO<sub>2</sub> (Fig. 4 (inset)), which should contribute to the enhancement of specific surface area.

### 3.5. XPS results

XPS technique was used to characterize the chemical state and the atomic concentrations of catalyst surface component. Fig. 5 shows XPS spectra of Fe 2p, Mo 3d, O 1s and Ce 3d, and the corresponding surface atomic concentrations and the relative atomic concentration ratios are summarized in Table 2. As for MoFe/Beta@CeO<sub>2</sub>, the surface concentration of Fe (1.14%) and Mo (0.21%) are found to be lower than those of CeMoFe/Beta (1.25% & 0.29%) and MoFe/Beta (1.34% & 0.33%). It indicates that Fe and Mo are within the cerium oxides layers, thus the corresponding photoelectrons intensity is lower. It is in good conformity to TEM analysis. Fig. 5A shows XPS results of Fe 2p<sub>3/2</sub> for MoFe/Beta@CeO<sub>2</sub> and MoFe/Beta catalysts. Peaks located near 712.5 and 710 eV can be assigned to  $Fe^{3+}$  and  $Fe^{2+}$ , respectively [38,39]. It indicates that the iron in our samples is present both as  $Fe^{2+}$  and  $Fe^{3+}$ . The results from deconvolution are presented in Table 2. It is noted that the surface  $Fe^{2+}/Fe^{3+}$  ratio increases about 9.7% after coating CeO<sub>2</sub> shell. As is well known,  $Fe^{2+}/Fe^{3+}$  redox-couples could promote the formation of oxygen vacancies and redox cycle. The more  $Fe^{2+}$ , the easier to form oxygen vacancies, and the more advantageous to the

adsorption of oxygen on catalyst surface to form chemisorbed oxygen species. In addition, Fe 2p spectra of MoFe/Beta@CeO<sub>2</sub> move slightly to the higher binding energy, demonstrating an interaction between iron oxide species and CeO<sub>2</sub> layers.

As shown in Fig. 5B, XPS spectra of Mo 3d were fitted into two peaks centered at 232.0 and 235.0 eV, which are attributed to MoO<sub>2</sub> and MoO<sub>3</sub>, respectively [40]. This result indicates that only Mo<sup>4+</sup> and Mo<sup>6+</sup> species are present on MoFe/Beta@CeO<sub>2</sub> and MoFe/Beta catalysts. Additionally, it can clearly be seen that Mo 3d spectra of MoFe/Beta@CeO<sub>2</sub> also shift slightly to higher binding energy.

Fig. 5C presents O 1s XPS spectra of MoFe/Beta@CeO<sub>2</sub>, CeMoFe/Beta, MoFe/Beta and pure CeO<sub>2</sub>, which were fitted into three peaks corresponding to the lattice oxygen  $O_\alpha$  (529.5–530.2 eV), chemisorbed oxygen  $O_\beta$  (531.4–531.7 eV) and hydroxyl groups  $O_\gamma$  (532.4–532.9 eV), respectively [41,42]. It's noted that a distinct increase of the intensities corresponding to  $O_\beta$  and  $O_\gamma$  have been observed after coating by CeO<sub>2</sub>. It can be clearly observed from Table 2 that the molar concentration of  $O_\beta$  on MoFe/Beta@CeO<sub>2</sub> (59.8%) is slightly higher than that on CeMoFe/Beta (57.6%) and MoFe/Beta (54.9%). It's been accepted that the  $O_\beta$  is the most active oxygen species and plays an important role in the redox reaction, and may contribute to the excellent NH<sub>3</sub>-SCR performance of MoFe/Beta@CeO<sub>2</sub>. In addition, Kwon et al. [23] found that the high ratio of surface chemisorbed oxygen was conducive to increase catalytic activity and SO<sub>2</sub> resistance. Furthermore, it is important to note that the amount of  $O_\gamma$  increases from 21.7% to 23.5% after CeO<sub>2</sub> sheath coating. It indicates the increase of

**Table 2**

The surface atomic concentrations of Fe, Mo, Ce, O and the relative concentration ratios.

Catalyst	surface atomic concentrations				relative concentration ratios		
	Fe	Mo	O	Ce	Fe <sup>2+</sup> /Fe	O <sub>γ</sub> /O	O <sub>β</sub> /O
MoFe/Beta@CeO <sub>2</sub>	1.14%	0.21%	38.69%	2.99%	58.4%	23.5%	59.8%
CeMoFe/Beta	1.25%	0.29%	32.26%	0.72%	48.6%	24.7%	57.6%
MoFe/Beta	1.34%	0.33%	28.34%		48.7%	21.7%	54.9%
CeO <sub>2</sub>			87.49%		12.51%	39.8%	38.9%

hydroxyl groups, which could serve as Brønsted acid sites to adsorb NH<sub>3</sub> and form NH<sup>4+</sup> and then react with NO<sub>2</sub> adsorbed nearby to produce N<sub>2</sub> and H<sub>2</sub>O during NH<sub>3</sub>-SCR process. Thus, it can enhance NH<sub>3</sub>-SCR performance. The last but not the least, it is noteworthy that the O 1s peak for MoFe/Beta@CeO<sub>2</sub> shifts to a higher binding energy compared with MoFe/Beta due to the interaction between the lattice oxygen and metal atoms, which may be conducive to the oxidation of NO to NO<sub>2</sub> in the SCR reaction [23,43]. Therefore, it facilitates the improvement of the low-temperature NH<sub>3</sub>-SCR performance.

Fig. 5D shows the Ce 3d XPS spectrum of MoFe/Beta@CeO<sub>2</sub>, CeMoFe/Beta and pure CeO<sub>2</sub>, which is split into ten peaks arising from Ce<sup>4+</sup>(u'', u'', u, v'', v' and v<sub>0</sub>) and Ce<sup>3+</sup>(u', u<sub>0</sub>, v'' and v) contributions [27,28]. It indicates that the coexistence of Ce<sup>3+</sup> and Ce<sup>4+</sup> in all of the three samples. In addition, Ce 3d<sub>3/2</sub> and Ce 3d<sub>5/2</sub> peaks of MoFe/Beta@CeO<sub>2</sub> shift slightly to the lower binding energies compared with the pristine CeO<sub>2</sub>, which can be ascribed to the interface effects between the core and shell. It indicates that there is a strong interaction between CeO<sub>2</sub> shell and MoFe/Beta core, which may play a synergistic role in the NH<sub>3</sub>-SCR reaction.

### 3.6. XANES results

In order to further explore the effect of the coating of CeO<sub>2</sub> shell on chemical state and coordination state of iron species, XANES experiment was performed in total electron yield mode. Prior to each test, the samples were mixed with graphite powders to increase electric conductivity and minimize charging effect. The Fe L<sub>3</sub>-edge XANES spectra of MoFe/Beta@CeO<sub>2</sub> and MoFe/Beta are shown in Fig. 6. Two distinct absorption peaks are observed at 706.8 eV (A<sub>1</sub>) and 708.8 eV (A<sub>2</sub>) due to the interplay of crystal field, spin-orbital and electronic interaction [44], which is consistent with the results reported by Yang, et al. [45]. Based on the charge transfer multiplet theory [46], the peaks at 706.8 eV (A<sub>1</sub>) and 708.8 eV (A<sub>2</sub>) correspond to the 2p<sub>3/2</sub> → 3d electron transition for Fe<sup>2+</sup> and Fe<sup>3+</sup>, respectively. Moreover, the absorption bands corresponding to Fe<sup>2+</sup> and Fe<sup>3+</sup> shift slightly to the higher photon energy, confirming the existence of electronic inductive effect between the coating of CeO<sub>2</sub> shell and MoFe/Beta core. Furthermore, the intensity ratios of A<sub>1</sub>/(A<sub>1</sub> + A<sub>2</sub>) for MoFe/Beta@CeO<sub>2</sub> and MoFe/Beta are calculated to be 0.47 and 0.36, respectively. The results reveal that in the two samples there coexist in comparable quantity both Fe<sup>2+</sup> and Fe<sup>3+</sup> states, and more importantly, MoFe/Beta coated by CeO<sub>2</sub> shell has significantly higher fraction of Fe<sup>2+</sup> than the uncoated one, which agrees well with the XPS results. Combined with XPS results, it demonstrates that the coating of CeO<sub>2</sub> shell significantly influence the ratio of Fe<sup>2+</sup>/Fe<sup>3+</sup> on MoFe/Beta@CeO<sub>2</sub> catalyst, and then the NH<sub>3</sub>-SCR performance may be regulated.

### 3.7. NH<sub>3</sub>-TPD results

It's widely accepted that the adsorption and activation of NH<sub>3</sub> molecule on the acid sites of catalyst surface are a primary process in NH<sub>3</sub>-SCR reaction. Therefore, NH<sub>3</sub>-TPD profiles were carried to investigate the effect of CeO<sub>2</sub> shell on the acidity of the catalysts, and the results are shown in Fig. 7. Both MoFe/Beta and CeO<sub>2</sub> cat-

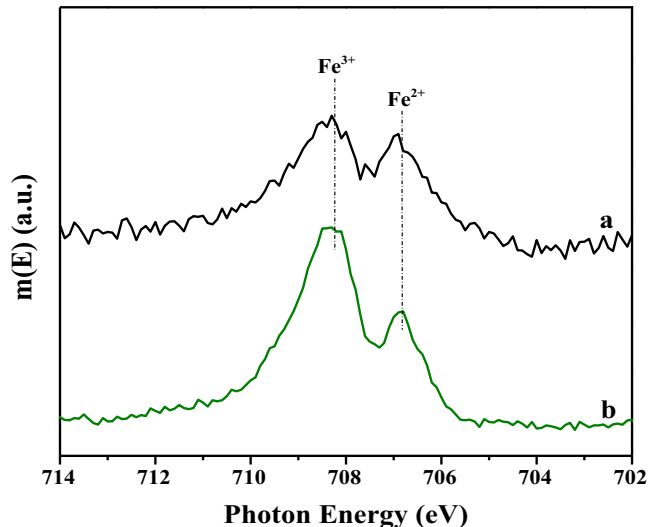


Fig. 6. XANES spectra of the catalysts: (a) MoFe/Beta@CeO<sub>2</sub> (b) MoFe/Beta.

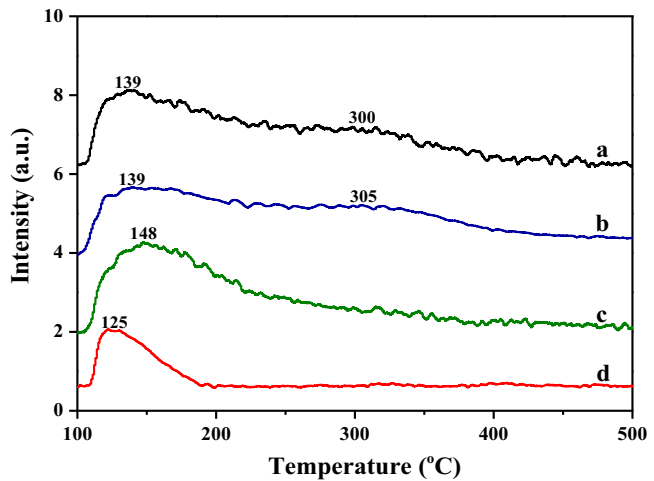
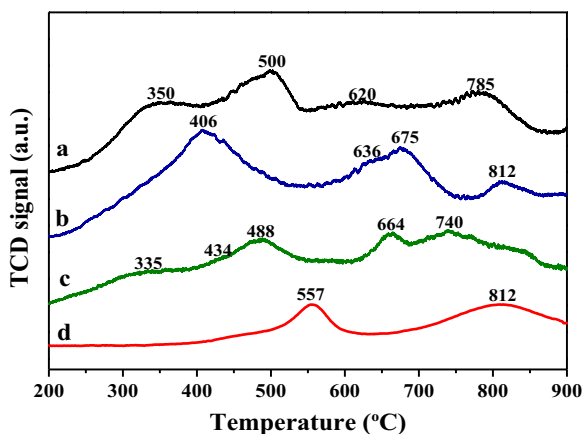


Fig. 7. NH<sub>3</sub>-TPD profiles of the catalysts: (a) MoFe/Beta@CeO<sub>2</sub> (b) CeMoFe/Beta (c) MoFe/Beta (d) CeO<sub>2</sub>.

alysts show one desorption peak at 148 and 125 °C, respectively. Whereas, for MoFe/Beta@CeO<sub>2</sub> core–shell catalyst, two distinct NH<sub>3</sub> desorption peaks are observed at 139 and 300 °C, which can be attributed to physisorbed NH<sub>3</sub> and/or ammonium species adsorbed at the weak acid sites and NH<sub>3</sub> adsorbed at the strong acid sites, respectively [47]. It has been demonstrated that the temperature of desorption peak reflects the acid strength of the catalyst, while the peak area represents the acid amount [27,48]. Consequently, it is evident that the acid amount and acid strength of strong acid sites have been enhanced after CeO<sub>2</sub> coating, which may be beneficial for the NH<sub>3</sub>-SCR reaction. Additionally, it's also noted that the acid amount and acid strength of weak acid sites decrease distinctly due to CeO<sub>2</sub> coating. It's well known that NH<sub>3</sub>-SCR reaction is an acid



**Fig. 8.** H<sub>2</sub>-TPR profiles of the catalysts: (a) MoFe/Beta@CeO<sub>2</sub> (b) CeMoFe/Beta (c) MoFe/Beta (d) CeO<sub>2</sub>.

catalysis and redox reaction. Although the acidity of the catalyst is not a crucial factor for high NH<sub>3</sub>-SCR activity, proper amount of it can promote SCR activity [49].

### 3.8. H<sub>2</sub>-TPR results

The redox property of catalyst plays a vitally important role in the catalytic process of NH<sub>3</sub>-SCR of NO. H<sub>2</sub>-TPR was employed to study the change of reducibility of the catalysts before and after coating by CeO<sub>2</sub> sheaths, and the results are displayed in Fig. 8. For CeO<sub>2</sub>, two broad reduction peaks are observed. The first one centered at 557 °C is ascribed to the reduction of surface capping oxygen, while the second one centered at 812 °C is assigned to bulk oxygen of ceria [50]. H<sub>2</sub>-TPR profile of MoFe/Beta presents five reduction peaks at 335, 434, 488, 664 and 740 °C, which can be attributed to the reduction of Fe<sub>2</sub>O<sub>3</sub> to Fe<sub>3</sub>O<sub>4</sub>, highly dispersed Mo species, Fe<sub>3</sub>O<sub>4</sub> to Fe, Fe<sub>3</sub>O<sub>4</sub> to FeO and FeO to Fe, respectively [4,51]. By contrast, after coating by CeO<sub>2</sub> shell, the reduction peak attributed to iron oxide and molybdenum oxide species shifted slightly to the higher temperature, which may be attributed to the interaction of CeO<sub>2</sub> sheaths with iron oxide and molybdenum oxide species. It agrees well with the results of XPS analysis. Additionally, it is worth noting that the peak corresponds to the reduction of iron oxide species becomes broader and stronger. It's generally accepted that the area of reduction peak is positively related to the amount of active species. Therefore, it demonstrates the increase of the iron oxide species that can be reduced or the increase of redox property of cerium oxide NPs, all of which are beneficial to the enhancement of NH<sub>3</sub>-SCR of NO. Furthermore, compared with MoFe/Beta@CeO<sub>2</sub> core–shell catalyst, CeMoFe/Beta exhibits a higher temperature corresponding to the reduction of iron oxide species. Combined with the above observations, it can be deduced that the interaction between iron oxide, molybdenum oxide and CeO<sub>2</sub> shells plays a synergistic role in the reducibility of the MoFe/Beta@CeO<sub>2</sub> core–shell catalysts, which could promote the activity of the catalyst in NH<sub>3</sub>-SCR reaction.

### 3.9. Catalytic performance results

In practical use, SO<sub>2</sub> is an important factor in the effluent gases from diesel engines influencing SCR activity over the catalysts. The trace amounts of SO<sub>2</sub> can result in the decrease of the catalytic performance [52]. Fig. 9A shows the NO<sub>x</sub> conversion of MoFe/Beta@CeO<sub>2</sub>, CeMoFe/Beta, MoFe/Beta, CeO<sub>2</sub> and Cu/SAPO-34 catalysts in the presence of 100 ppm SO<sub>2</sub> in the range of 100–600 °C under the GHSV of 50,000 h<sup>-1</sup>. It can be observed that the NO<sub>x</sub>

conversion changes with the increase of reaction temperature. For pure CeO<sub>2</sub>, the maximum NO<sub>x</sub> conversion is only 73.5% at 400 °C in the whole temperature range. MoFe/Beta@CeO<sub>2</sub> exhibits a higher low-temperature NO<sub>x</sub> conversion and a wider operation temperature window than the other catalysts. The NO<sub>x</sub> conversion is above 90% in the range of 225–600 °C over MoFe/Beta@CeO<sub>2</sub> catalyst. While for MoFe/Beta, the NO<sub>x</sub> conversion reaches to 90% nearly at 300 °C and dramatically decreases when the reaction temperature is beyond 500 °C. It may be due to the migration and agglomeration of the metal oxides at high temperature, leading to the deactivation of catalysts. By contrast, MoFe/Beta@CeO<sub>2</sub> catalyst exhibits more robust at corresponding conditions. In addition, it can also be seen that the low-temperature NH<sub>3</sub>-SCR performance of CeMoFe/Beta was improved to some extent compared to MoFe/Beta. However, the NO<sub>x</sub> conversion gradually declines when the reaction temperature is over 450 °C, which may be due to the presence of bigger CeO<sub>2</sub> NPs (as shown in Fig. 3b), aggravating the unselective oxidation of NH<sub>3</sub>. Cu/SAPO-34, a representative NH<sub>3</sub>-SCR zeolite catalyst, was also conducted for the purpose of comparison. It can be seen that Cu/SAPO-34 catalyst exhibited a relatively lower NO<sub>x</sub> conversion compared with MoFe/Beta in the whole temperature range, revealing that MoFe/Beta exhibits better SO<sub>2</sub>-tolerance than Cu/SAPO-34 catalyst. According to the above observations, it can be concluded that CeO<sub>2</sub> sheaths have effectively suppressed the formation of ammonium sulfate species blocking the active sites and prevented SO<sub>2</sub> from poisoning active phases over MoFe/Beta@CeO<sub>2</sub> catalyst at low temperature. The migration and aggregation of the active metal oxides are prevented at high temperature (>450 °C). Thus, the stability of the catalyst is enhanced. The excellently catalytic activity of MoFe/Beta@CeO<sub>2</sub> catalyst could be ascribed to the core–shell structure of CeO<sub>2</sub> coating MoFe/Beta.

The N<sub>2</sub> selectivity is a crucial role in evaluating the catalytic activity of SCR catalyst. As shown in Fig. 9B, nearly 100% N<sub>2</sub> selectivity was obtained over MoFe/Beta@CeO<sub>2</sub>, CeMoFe/Beta, MoFe/Beta and Cu/SAPO-34 catalysts in the whole temperature range of 100–600 °C. However, in the case of CeO<sub>2</sub>, the N<sub>2</sub> selectivity remarkably decreased as reaction temperature is above 300 °C, which should be due to the unselective catalytic oxidation of NH<sub>3</sub> to N<sub>2</sub>O and/or NO.

As an important indicator of evaluation the performance of catalysis, the catalytic stability of the catalysts before and after CeO<sub>2</sub> coating is investigated. Fig. 9C shows the stability tests of the catalysts in the presence of 100 ppm SO<sub>2</sub> as a function of time at 300 °C. Surprisingly, it can be noted that the catalytic performance of MoFe/Beta@CeO<sub>2</sub> catalyst is barely affected by SO<sub>2</sub> in the feed gas, and the NO<sub>x</sub> conversion over the catalyst still maintains at around 98% after 25 h tested, indicating the high resistance ability of MoFe/Beta@CeO<sub>2</sub> catalyst to SO<sub>2</sub> poisoning. For CeMoFe/Beta, the NO<sub>x</sub> conversion gradually declines with the time on stream and decreases to about 6% after 25 h. In sharp contrast, the deNO<sub>x</sub> activity of MoFe/Beta sharply drops within 4 h and decreases to 77% after 25 h. While for Cu/SAPO-34, it can be seen that NO<sub>x</sub> conversion dramatically declines within 2 h and decreases to 62% after 4 h. SO<sub>2</sub> resulting in catalyst poisoning and deactivation derives from the following two aspects. On the one hand, the reaction of SO<sub>2</sub> and NH<sub>3</sub> generates ammonium sulfate species depositing on the catalyst surface and blocking the active sites of the catalyst surface, which can result in a gradual decrease of NO<sub>x</sub> conversion. The deactivation of the catalyst resulted from this process is reversible. On the other hand, the active phases of the catalyst react with SO<sub>2</sub> to form stable sulfated species leading to a rapid decrease of NO<sub>x</sub> conversion, which results in an irreversible deactivation [53]. Therefore, it can be concluded that compared to CeMoFe/Beta catalyst, MoFe/Beta@CeO<sub>2</sub> shows a remarkable resistance to SO<sub>2</sub> due to the protection of CeO<sub>2</sub> shell.

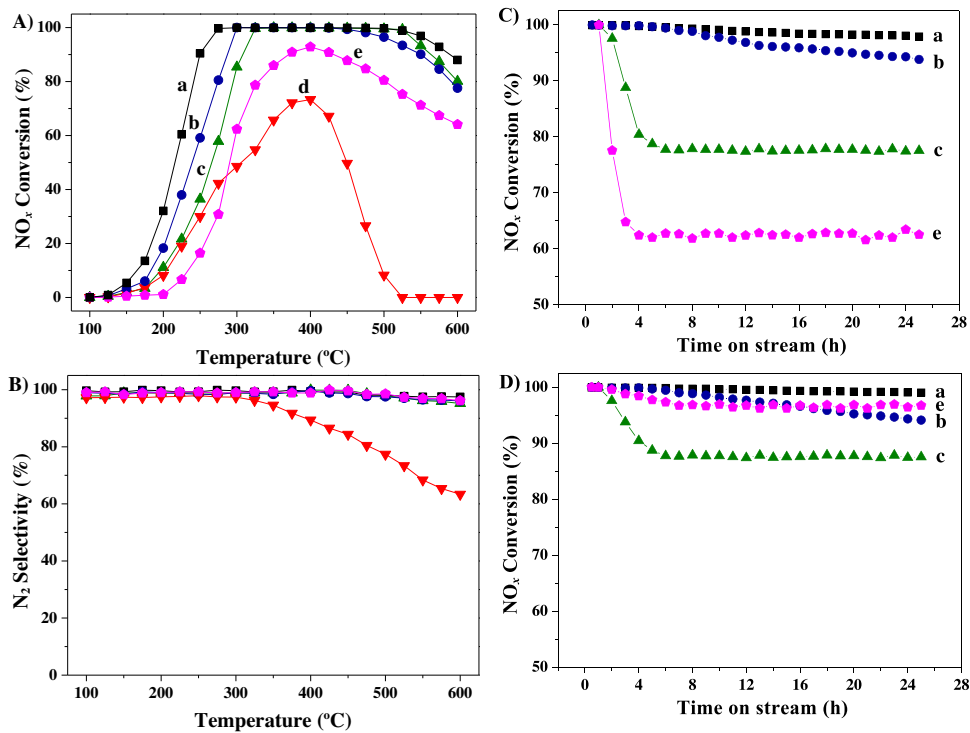


**Fig. 9.** (A)  $\text{NO}_x$  conversion and (B)  $\text{N}_2$  selectivity in the presence of  $\text{SO}_2$ : (a) MoFe/Beta@CeO<sub>2</sub> (b) CeMoFe/Beta (c) MoFe/Beta (d) CeO<sub>2</sub> (e) Cu/SAPO-34 (C) Tests of  $\text{SO}_2$  resistance and (D) Tests of  $\text{H}_2\text{O}$  resistance at 300 °C: (a) MoFe/Beta@CeO<sub>2</sub> (b) CeMoFe/Beta (c) MoFe/Beta (e) Cu/SAPO-34. Reaction conditions:  $[\text{NO}] = [\text{NH}_3] = 500 \text{ ppm}$ ,  $[\text{SO}_2] = 100 \text{ ppm}$ ,  $[\text{O}_2] = 3 \text{ vol\%}$ ,  $[\text{H}_2\text{O}] = 10\%$ ,  $\text{N}_2$  balance and GHSV = 50,000  $\text{h}^{-1}$ .

The effect of  $\text{H}_2\text{O}$  on the SCR activity over MoFe/Beta@CeO<sub>2</sub>, CeMoFe/Beta and MoFe/Beta as a function of time at 300 °C was also investigated, and the results were exhibited in Fig. 9D. It can be found that MoFe/Beta@CeO<sub>2</sub> catalyst exhibits the best NH<sub>3</sub>-SCR performance with  $\text{NO}_x$  conversion above 99% in the whole test range in the presence of 10%  $\text{H}_2\text{O}$ . For MoFe/Beta, the  $\text{NO}_x$  conversion rapidly decreases to around 87% after 6 h, which may be due to the aggregation of active metals and/or the structure collapsed of support [54]. While for CeMoFe/Beta, the  $\text{NO}_x$  conversion is somewhat improved compared with MoFe/Beta catalyst and is still lower than MoFe/Beta@CeO<sub>2</sub>. It indicates high  $\text{H}_2\text{O}$  resistance ability of MoFe/Beta@CeO<sub>2</sub> core–shell catalyst.

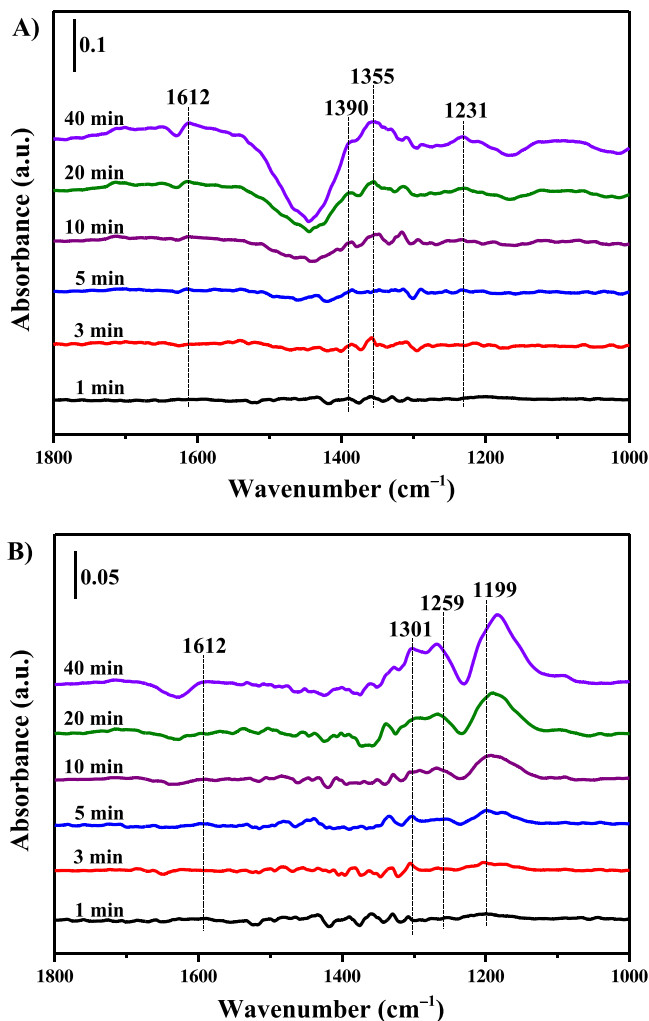
It was reported that the presence of  $\text{SO}_2$  had a great effect on NO adsorption and oxidation in SCR reaction, which could form sulfate species ( $(\text{NH}_4)_2\text{SO}_4$  and  $\text{NH}_4\text{HSO}_4$ ) blocking the active sites for NO oxidation and then cut off the reaction pathway [6,55,56]. The in-situ DRIFTS spectra of co-adsorption of  $\text{NO} + \text{O}_2$  over MoFe/Beta@CeO<sub>2</sub> and MoFe/Beta catalysts after  $\text{SO}_2$  tolerance test at 200 °C are investigated and the results are displayed in Fig. 10. It can be noted from Fig. 10A that several distinct bands appear at 1612, 1390, 1355 and 1231  $\text{cm}^{-1}$  after 40 min of exposure, which are assigned to asymmetric stretching vibration of gaseous  $\text{NO}_2$ , *trans*- $\text{N}_2\text{O}_2^2$ , linear nitrites and monodentate nitrate, respectively [57–59]. The intensity of these peaks gradually enhances with the time. According to the above observations, it can be inferred that the formation of  $\text{NO}_2$  and nitrites species, to some degree, can account for the high de $\text{NO}_x$  performance of MoFe/Beta@CeO<sub>2</sub> at the low temperature.

Fig. 10B exhibits the in-situ DRIFT spectra of  $\text{NO} + \text{O}_2$  co-adsorption on MoFe/Beta catalyst, which is different from that of MoFe/Beta@CeO<sub>2</sub>. Three distinct bands are observed at 1301, 1259 and 1199  $\text{cm}^{-1}$ , which can be ascribed to monodentate nitrate, monodentate nitrite and bridging nitrate, respectively [43,47]. It has been accepted that the formation of nitrate species is unfavorable for the NH<sub>3</sub>-SCR reaction, which is very stable and can cover the

active sites resulting in the decrease of NH<sub>3</sub>-SCR performance [58]. Furthermore, it is important to note that the intensity of the band at 1612  $\text{cm}^{-1}$  ascribed to gaseous  $\text{NO}_2$  is much lower than that of MoFe/Beta@CeO<sub>2</sub>. According to the above observation, it from a side proves that CeO<sub>2</sub> shells have considerably suppressed the formation of sulfate species and ammonium nitrate blocking the active iron sites. Moreover, It also demonstrates that CeO<sub>2</sub> shell coating catalyst not only inhibit the formation of nitrate species from covering the active iron sites but also can promote the generation of nitrites species and  $\text{NO}_2$  during NH<sub>3</sub>-SCR, and then enhance the NH<sub>3</sub>-SCR performance.

Combined with the above observations, it can be concluded that ceria-shell functions as a protective layer greatly enhanced the NH<sub>3</sub>-SCR performance, thermal stability and  $\text{SO}_2/\text{H}_2\text{O}$ -tolerance of MoFe/Beta catalyst. The reasons may be as following: Firstly, owing to the presence of ceria-shell functions serving as a protective layer,  $\text{SO}_2$  can't directly react with active component on MoFe/Beta@CeO<sub>2</sub> catalyst to produce inactive sulfate species. Therefore, the active iron sites were protected and then the low-temperature performance of MoFe/Beta@CeO<sub>2</sub> catalyst was enhanced. Secondly, because of the presence of strong interaction among the iron oxides, molybdenum oxides and CeO<sub>2</sub> shells (confirmed by XPS and H<sub>2</sub>-TPR), CeO<sub>2</sub> shells can serve as an effective barrier to inhibit the active metal oxides nanoparticles from aggregating at high temperature. As a result, the coated catalyst with CeO<sub>2</sub> thin film shows an improved thermal stability. Finally, the formation of sulfated ceria species may increase the amount of surface active oxygen and surface hydroxyls, which is beneficial to improving the ability of NO oxidation to  $\text{NO}_2$  and then promoting the “fast SCR” process during NH<sub>3</sub>-SCR [6].

Presumably CeO<sub>2</sub> gradually transforms to  $\text{Ce}(\text{SO}_4)_2$ , but what happens when the transformation is complete? Indeed, this phenomenon would happen that CeO<sub>2</sub> gradually transforms to  $\text{Ce}(\text{SO}_4)_2$  in the presence of  $\text{SO}_2$ , which has been reported by many researchers. But it is slightly different in this work. First of all,



**Fig. 10.** In situ DRIFTS spectra of  $\text{NO} + \text{O}_2$  adsorption on sulfated catalysts measured at  $200^\circ\text{C}$  (A) MoFe/Beta@CeO<sub>2</sub> (B) MoFe/Beta.

MoFe/Beta@CeO<sub>2</sub> catalyst is protected by the outer CeO<sub>2</sub> shell, which is about 10 nm. Although, CeO<sub>2</sub> gradually transforms to Ce(SO<sub>4</sub>)<sub>2</sub> and even completely transformation along with the process of SCR reaction, “CeO<sub>2</sub> shells” can still inhibit the ammonium nitrate and sulfate species (NH<sub>4</sub>HSO<sub>4</sub>) formed in this SCR process from depositing on the surface of catalyst and blocking the active iron sites over MoFe/Beta@CeO<sub>2</sub> catalyst, and then guaranteeing the reaction smoothly. What's more, CeO<sub>2</sub> shells can still serve as an effective barrier to inhibit the active metal oxides nanoparticles from aggregating at high temperature. Therefore, the coated catalyst with CeO<sub>2</sub> thin film can show an improved thermal stability. The last but not the least, even though CeO<sub>2</sub> gradually transforms to Ce(SO<sub>4</sub>)<sub>2</sub>, on the one hand, the formation of Ce(SO<sub>4</sub>)<sub>2</sub> could increase the amount of surface active oxygen species, and then promote the ability of NO oxidation to NO<sub>2</sub>. On the other hand, the amount of surface hydroxyls due to the hydration of SO<sub>4</sub><sup>2-</sup> may be increased, which could supply more Brønsted acid sites to adsorb NH<sub>3</sub> in the form of NH<sub>4</sub><sup>+</sup>. The both factors played significant roles in the good SO<sub>2</sub> durability of SCR catalyst. Certainly, as the CeO<sub>2</sub> shell completely transforms to Ce(SO<sub>4</sub>)<sub>2</sub>, SO<sub>2</sub> would gradually react with active component over MoFe/Beta@CeO<sub>2</sub> catalyst to generate inactive sulfate species, resulting in deactivation of the catalyst. In summary, it has to say that this work lays a foundation for guiding the development of highly active NH<sub>3</sub>-SCR catalysts core–shell structure.

#### 4. Conclusions

We have designed a new MoFe/Beta@CeO<sub>2</sub> core–shell catalyst with nano-size Beta supporting MoFe bimetallic oxides as the core and CeO<sub>2</sub> thin film as the shell. MoFe/Beta@CeO<sub>2</sub> catalyst exhibits higher catalytic performances, higher stability, H<sub>2</sub>O and SO<sub>2</sub>-tolerance than either pure CeO<sub>2</sub> or MoFe/Beta for NH<sub>3</sub>-SCR reaction. The NO<sub>x</sub> conversion is above 90% in the temperature range of 225–600 °C over MoFe/Beta@CeO<sub>2</sub> catalyst even if the reaction gases include 100 ppm SO<sub>2</sub>. It can be ascribed to the interface effects between the core (MoFe/Beta) and shell (CeO<sub>2</sub>).

The interface effects between the molybdenum oxide, iron oxide and CeO<sub>2</sub> sheaths have not only restrained the formation of ammonium sulfate and nitrate species from blocking the active sites but also prevented the generation of iron sulfate, leading to a high SO<sub>2</sub>-tolerance. Moreover, CeO<sub>2</sub> shells have served as an effective barrier to suppress the migration and aggregation of active metal oxides and thus enhance the thermal stability. Furthermore, the CeO<sub>2</sub> shell coating catalyst not only can promote the formation of nitrites species but also strengthen the acidity of catalyst and promote NO oxidation to NO<sub>2</sub>, which may be an important factor accounting for the high catalytic performances of MoFe/Beta@CeO<sub>2</sub> core–shell catalyst. Therefore, the present work lays a foundation for guiding the development of highly active NH<sub>3</sub>-SCR catalysts and the design and application of core–shell catalysts.

#### Acknowledgements

This work was financially supported by the National Natural Science Foundation of China (21673290 and 21376261), 863 Program of China (2015AA034603), the Beijing Natural Science Foundation (2142027), and the China University of Petroleum Fund (20130007110007 and 2462015QZDX04).

#### References

- [1] J.O. Barth, A. Jentys, J.A. Lercher, *Ind. Eng. Chem. Res.* 43 (2004) 3097–3104.
- [2] A. Boubnov, H.W.P. Carvalho, D.E. Doronkin, T. Guenter, E. Gallo, A.J. Atkins, C.R. Jacob, J.D. Grunwaldt, *J. Am. Chem. Soc.* 136 (2014) 13006–13015.
- [3] E. Garcia-Bordejé, J.L. Pinilla, M.J. Lazaro, R. Moliner, *Appl. Catal. B* 66 (2006) 281–287.
- [4] P. Balle, B. Geiger, S. Kureti, *Appl. Catal. B* 85 (2009) 109–119.
- [5] J.P. Dunn, P.R. Koppula, H.G. Stenger, I.E. Wachs, *Appl. Catal. B* 19 (1998) 103–117.
- [6] Y. Shu, T. Aikebaier, X. Quan, S. Chen, H. Yu, *Appl. Catal. B* 150 (2014) 630–635.
- [7] P. Sazama, B. Wichterlova, S. Sklenak, V.I. Parvulescu, N. Candu, G. Sadovska, J. Dedecek, P. Klein, V. Pashkova, P. Stastny, *J. Catal.* 318 (2014) 22–33.
- [8] T. Zhang, J. Li, J. Liu, D. Wang, Z. Zhao, K. Cheng, J. Li, *AIChE J.* 61 (2015) 3825–3837.
- [9] S. Andonova, S. Tamm, C. Montreuil, C. Lambert, L. Olsson, *Appl. Catal. B* 180 (2016) 775–787.
- [10] T. Zhang, J. Liu, D. Wang, Z. Zhao, Y. Wei, K. Cheng, G. Jiang, A. Duan, *Appl. Catal. B* 148–149 (2014) 520–531.
- [11] R. Delahay, S. Kieger, N. Tanchoux, P. Trens, B. Coq, *Appl. Catal. B* 52 (2004) 251–257.
- [12] O. Mihai, C.R. Widjyastuti, S. Andonova, K. Kamasamudram, J. Li, S.Y. Joshi, N.W. Currier, A. Yezersets, L. Olsson, *J. Catal.* 311 (2014) 170–181.
- [13] X. Zhang, Q. Shen, C. He, C. Ma, J. Cheng, L. Li, Z. Hao, *ACS Catal.* 2 (2012) 512–520.
- [14] P.J. Jodlowski, J. Kryca, A. Rogulska, B. Gil, M. Iwaniszyn, J. Lojewska, A. Kolodziej, *Chem. Eng. J.* 214 (2013) 319–326.
- [15] R. Foo, T. Vazhnova, D.B. Lukyanov, P. Millington, J. Collier, R. Rajaram, S. Golunski, *Appl. Catal. B* 162 (2015) 174–179.
- [16] K. Gora-Marek, K. Brylewsk, K.A. Tarach, M. Rutkowska, M. Jablonska, M. Choi, L. Chmielarz, *Appl. Catal. B* 179 (2015) 589–598.
- [17] S. Shwan, L. Olsson, M. Skoglundh, J. Jansson, *AIChE J.* 61 (2015) 215–223.
- [18] S.Y. Jiang, R.X. Zhou, *Fuel Process. Technol.* 133 (2015) 220–226.
- [19] Y.J. Kim, H.J. Kwon, I. Heo, I.S. Nam, B.K. Cho, J.W. Choung, M.S. Cha, G.K. Yeo, *Appl. Catal. B* 126 (2012) 9–21.
- [20] J.D. Han, *Clean Technol.* 21 (2015) 153–163.
- [21] E.J.M. Hensen, P.J. Kooyman, Y. van der Meer, A.M. van der Kraan, V.H.J. de Beer, J.A.R. van Veen, R.A. van Santen, *J. Catal.* 199 (2001) 224–235.
- [22] Y.Y. Shu, R. Ohnishi, M. Ichikawa, *J. Catal.* 206 (2002) 134–142.
- [23] D.W. Kwon, K.H. Park, S.C. Hong, *Chem. Eng. J.* 284 (2016) 315–324.
- [24] R.G. Chaudhuri, S. Paria, *Chem. Rev.* 112 (2012) 2373–2433.

[25] M.B. Gawande, A. Goswami, T. Asefa, H. Guo, A.V. Biradar, D.L. Peng, R. Zboril, R.S. Varma, *Chem. Soc. Rev.* 44 (2015) 7540–7590.

[26] T. Mitsudome, Y. Mikami, M. Matoba, T. Mizugaki, K. Jitsukawa, K. Kaneda, *Angew. Chem. Int. Ed.* 51 (2012) 136–139.

[27] L. Zhang, D. Zhang, J. Zhang, S. Cai, C. Fang, L. Huang, H. Li, R. Gao, L. Shi, *Nanoscale* 5 (2013) 9821–9829.

[28] S. Cai, H. Hu, H. Li, L. Shi, D. Zhang, *Nanoscale* 8 (2016) 3588–3598.

[29] Z. Wu, M. Li, S.H. Overbury, *J. Catal.* 285 (2012) 61–73.

[30] M. Li, Z. Wu, S.H. Overbury, *J. Catal.* 306 (2013) 164–176.

[31] M. Honda, M. Tamura, Y. Nakagawa, K. Nakao, K. Suzuki, K. Tomishige, *J. Catal.* 318 (2014) 95–107.

[32] M.D. Krcha, K.M. Dooley, M.J. Janik, *J. Catal.* 330 (2015) 167–176.

[33] F. Gao, E.D. Walter, N.M. Washton, J. Szanyi, C.H.F. Peden, *Appl. Catal. B* 162 (2015) 501–514.

[34] H. Huang, Y. Gu, J. Zhao, X. Wang, *J. Catal.* 326 (2015) 54–68.

[35] P. Sudarsanan, B. Hillary, M.H. Amin, S.B.A. Hamid, S.K. Bhargava, *Appl. Catal. B* 185 (2016) 213–224.

[36] H. Bao, Z. Zhang, Q. Hua, W. Huang, *Langmuir* 30 (2014) 6427–6436.

[37] D. Zhang, A. Duan, Z. Zhao, C. Xu, *J. Catal.* 274 (2010) 273–286.

[38] F. Liu, H. He, Z. Lian, W. Shan, L. Xie, K. Asakura, W. Yang, H. Deng, *J. Catal.* 307 (2013) 340–351.

[39] S. Shwan, J. Jansson, L. Olsson, M. Skoglundh, *Appl. Catal. B* 166 (2015) 277–286.

[40] W. Lai, Z. Chen, J. Zhu, L. Yang, J. Zheng, X. Yi, W. Fang, *Nanoscale* 8 (2016) 3823–3833.

[41] S. Shwan, R. Nedyalkova, J. Jansson, J. Korsgren, L. Olsson, M. Skoglundh, *Ind. Eng. Chem. Res.* 51 (2012) 12762–12772.

[42] X. Li, J. Li, Y. Peng, H. Chang, T. Zhang, S. Zhao, W. Si, J. Hao, *Appl. Catal. B* 184 (2016) 246–257.

[43] H. Chang, X. Chen, J. Li, L. Ma, C. Wang, C. Liu, J.W. Schwank, J. Hao, *Environ. Sci. Technol.* 47 (2013) 5294–5301.

[44] P.S. Miedema, F.M.F. de Groot, *J. Electron Spectrosc. Relat. Phenom.* 187 (2013) 32–48.

[45] S.L. Yang, D.N. Wang, G.X. Liang, Y.M. Yiu, J.J. Wang, L.J. Liu, X.L. Sun, T.K. Sham, *Energy Environ. Sci.* 5 (2012) 7007–7016.

[46] F. de Groot, *Coordin. Chem. Rev.* 249 (2005) 31–63.

[47] Y. Miyamoto, N. Katada, M. Niwa, *Microporous Mesoporous Mat.* 40 (2000) 271–281.

[48] J. Liu, W. Song, C. Xu, J. Liu, Z. Zhao, Y. Wei, A. Duan, G. Jiang, *RSC Adv.* 5 (2015) 104923–104931.

[49] S. Brandenberger, O. Kröcher, A. Wokaun, A. Tissler, R. Althoff, *J. Catal.* 268 (2009) 297–306.

[50] W. Deng, Q. Dai, Y. Lao, B. Shi, X. Wang, *Appl. Catal. B* 181 (2016) 848–861.

[51] G. Delahay, D. Valade, A. Guzman-Vargas, B. Coq, *Appl. Catal. B* 55 (2005) 149–155.

[52] K. Skalska, J.S. Miller, S. Ledakowicz, *Sci. Total Environ.* 408 (2010) 3976–3989.

[53] B. Jiang, B. Deng, Z. Zhang, Z. Wu, X. Tang, S. Yao, H. Lu, *J. Phys. Chem. C* 118 (2014) 14866–14875.

[54] X. Shi, F. Liu, L. Xie, W. Shan, H. He, *Environ. Sci. Technol.* 47 (2013) 3293–3298.

[55] W. Xu, H. He, Y. Yu, *J. Phys. Chem. C* 113 (2009) 4426–4432.

[56] W. Yang, F. Liu, L. Xie, Z. Lian, H. He, *Ind. Eng. Chem. Res.* 55 (2016) 2677–2685.

[57] J. Li, R. Zhu, Y. Cheng, C.K. Lambert, R.T. Yang, *Environ. Sci. Technol.* 44 (2010) 1799–1805.

[58] L. Ma, J. Li, Y. Cheng, C.K. Lambert, L. Fu, *Environ. Sci. Technol.* 46 (2012) 1747–1754.

[59] C. Sedlmair, K. Seshan, A. Jentys, J.A. Lercher, *J. Catal.* 214 (2003) 308–316.